CHAPTER II
THEORETICAL BACKGROUND AND LITERATURE REVIEW

2.1 Enhanced Oil Recovery

Oil recovery operations traditionally have been subdivided into three stages: primary, secondary, and tertiary. Primary recovery, the initial production stage, is oil recovery by natural drive mechanisms existing in a reservoir such as solution gas, water influx, gas cap drive, or gravity drainage. Secondary recovery, the second stage of operations, is usually performed after the primary recovery has declined. The purpose of secondary recovery processes is to maintain reservoir pressure through waterflooding or gas injection. Tertiary recovery, the third stage of production, is any technique which uses miscible gases, chemicals, and/or thermal energy to displace additional oil after secondary recovery processes become uneconomical. As petroleum engineering has developed, however, this distinction has become less well defined. Many reservoir production operations are not conducted in the above specified order. Therefore, "enhanced oil recovery" (EOR) is a widely used term instead of tertiary recovery and it can be employed during more than one stage of recovery (Green and Willhite, 1998).

EOR processes involve the injection of liquid chemicals into the reservoir, including polymers, surfactants, and hydrocarbon solvents. The injected fluids and injection processes supplement the natural energy present in the reservoir to drive oil to a producing well. In addition, the injected fluids interact with the reservoir rock/oil system to create conditions favorable for oil recovery. These interactions might, for example, result in lower interfacial tension (IFT) permeabilities, oil swelling, oil viscosity reduction, wettability modification, or favorable phase behavior (Green and Willhite, 1998).

Polymer flooding, a type of chemical flooding, is one way to control drive-water mobility and fluid flow patterns in reservoirs. Polymers — long, chainlike, high-weight molecules — have three important oil recovery properties. They increase water viscosity, decrease effective rock permeability, and are able to change their viscosity with the flow rate. Small amounts of water-dissolved polymers increase the

viscosity of water. This higher viscosity slows the progress of the water flow through a reservoir and makes it less likely to bypass the oil in low-permeability rock (Gerding, 1986).

Table 2.1 gives a comparison of waterflooding and polymer flooding with a brief description of each process and its main use.

Table 2.1 Comparison of waterflooding and polymer flooding (Gerding, 1986)

Method of Recovery	Process	Use
Waterflooding	Water is pumped into the reservoir through injection wells to force oil toward production wells.	Method most widely used in secondary recovery.
Polymer Flooding	Water thickened with polymers is used to aid waterflooding by improving fluid-flow patterns.	As agents to lower water mobility in EOR processes.

2.2 Core Analysis

Core analysis is the laboratory measurement of the physico-chemical properties of samples of recovered core, for purposes of calibrating the interpretation of logging measurements or establishing the algorithms needed for more comprehensive petrophysical interpretation, and of fluid flow characteristics, for reservoir-engineering applications. For greater effectiveness, at least a subset of these measurements should be made at reservoir conditions of temperature and pressure (Dawe, 2000).

Core analysis can be divided into two categories: basic core analysis and special core analysis. Basic core analysis provides information on lithology, residual fluid saturation, ambient porosity, ambient air permeability (horizontal and vertical) and grain density. Special core analysis typically provides information on porosity

and permeability at elevated confining stresses, capillary pressure, electrical properties such as formation factor and resistivity index, wettability and relative permeability, mechanical rock properties such as compressibility and waterflood sensitivity for injectivity and well performance. The term "advanced core analysis" is used by some core analysis contractors to include the above special core analysis activities, as well as more recent advances in core analysis; for example, core nuclear magnetic resonance (NMR) measurements, multi-phase flow imaging and numerical modeling (Dawe, 2000).

2.3 Petrophysical Properties

Petrophysical properties comprise the physical properties of rocks and the fluids contained within them. Such studies are fundamental in the petroleum industry to evaluate hydrocarbon reservoirs and predict oil recovery.

2.3.1 Porosity

Porosity is a measure of the storage capacity of a reservoir. It is defined as the ratio of pore volume to bulk volume, and it can be calculated if two of the three intrinsic volumes (pore volume, grain volume, and bulk volume) are known. In equation form:

$$\phi = \frac{pore\ volume}{bulk\ volume} = \frac{bulk\ volume - grain\ volume}{bulk\ volume} \qquad (1)$$

For most naturally occurring media, the porosity can range from about 0.10 to 0.40 although, on occasion, values outside this range have been observed. Porosity is often reported as a percent, but in calculations it should always be used as a fraction. From these typical values, the rock phase clearly occupies the largest volume in any medium. The porosity of a permeable medium is a strong function of the variance of the local pore or grain size distribution and a weak function of the average pore size itself (Lake,1989).

Two types of porosity may be measured: total or absolute porosity and effective porosity. Total porosity is the ratio of all the pore spaces in the rock to the

bulk volume of the rock. Effective porosity, ϕ_e is the ratio of interconnected void spaces to the bulk volume. Thus, only the effective porosity contains fluids that can be recovered from wells. For granular materials such as sandstone, the effective porosity may approach the total porosity, however for shales and for highly cemented rocks such as some limestones, large deviations may exist between the two porosity (Torsæter and Abtahi, 1996).

Porosity may be classified according to its origin as either primary or secondary. Primary or original porosity is developed during deposition of the sediment. Secondary porosity is caused by some geological processes subsequent to the formation of the deposit. These changes in the original pore spaces may be created by ground stresses, water movement, or various other types of geological activities after the original sediments were deposited. Fracturing or formation of solution cavities often will increase the original porosity of the rock (Torsæter and Abtahi, 1996).

A liquid saturating method is used for porosity measurement on core samples in this work. The pores of a prepared sample are filled with a liquid of known density. The weight increase of the sample divided by the fluid density is a measure of the pore volume. This method gives interconnected porosity (Dawe, 2000).

2.3.2 Permeability

Permeability is a property of the porous medium and is a quantitative measure of the medium's ability to transmit fluids under a potential gradient. Permeability is a tensorial property that is, in general, a function of position and pressure. Usually, the pressure dependence is neglected in reservoir calculations, but the variation with position can be pronounced. Very often the permeability varies by several orders of magnitude, and such heterogeneity will of course influence any oil recovery. Permeability of a medium is a strong function of the local pore size and a weak function of the grain size distribution (Lake, 1989).

For single-phase, incompressible, horizontal fluid flow through a porous medium, Darcy's Law states that:

$$q = \frac{kA}{\mu}\frac{\Delta p}{L} \qquad (2)$$

where (in Darcy unit system) q is the flow rate, in cm^3/s, k is the permeability, in Darcys, A is the cross sectional area, in cm^2, μ is the fluid viscosity, in centipoises or cp, Δp is the pressure differential, in atmospheres, and L is the length, in cm (Dawe, 2000).

$$k[D] = \frac{q[cm^3/s] \cdot \mu[cP] \cdot L[cm]}{\Delta p[atm] \cdot A[cm^2]} \tag{3}$$

From the unit expression in Eq. (3), one Darcy is defined as the permeability that will permit a fluid of one centipoise viscosity to flow at a rate of one cubic centimeter per second through a cross-sectional area of one square centimeter when the pressure gradient is one atmosphere per centimeter. The millidarcy (mD), which is one thousandth (1/1000) of a Darcy (D), is used in core analysis and field calculations. Formation permeabilities vary from a fraction of one mD to more than 10000 mD (Dawe, 2000).

Permeability is measured by passing a fluid of known viscosity through a core sample of measured dimensions and then measuring flow rate and pressure drop. Darcy's equation suggests that a plot of q/A against pressure gradient ($\Delta p/L$) should yield a straight line, where the slope, k/μ, is the fluid mobility (Dawe, 2000).

For the channel system, the permeability can be estimated by the combination of Poiseuille's Law for capillary flow and Darcy's Law for flow of liquids in permeable beds (Beaumont and Foster, 1987).

Poiseuille's Law for viscous flow of liquids through capillary tubes:

$$q = \frac{\pi r^4 (p_1 - p_2)}{8 \mu L} \tag{4}$$

For an alternative set of units, Darcy's Law for steady state linear flow of incompressible fluids can be written as:

$$q = \frac{9.86 \cdot 10^{-9} k A (p_1 - p_2)}{\mu L} \tag{5}$$

Combination of Eq. (4) and (5) leads to

$$k = \frac{A r^2 (p_1 - p_2)}{8 \mu L} \cdot \frac{\mu L}{9.86 \cdot 10^{-9} A (p_1 - p_2)} \tag{6}$$

Therefore, $$k = 12.5 \cdot 10^6 r^2 \tag{7}$$

where q is the flow rate, in cm^3/s, k is the permeability, in Darcys, A is the cross sectional area, in cm^2, r is the channel radius, in cm, p_1-p_2 is the pressure differential, in $dynes/cm^2$, μ is the fluid viscosity, in poises, and L is the length, in cm (Beaumont and Foster, 1987).

If the inside radius is in inches rather than centimeters, the permeability is given by:

$$k = 80 \cdot 10^6 r^2 = 20 \cdot 10^6 D^2 \tag{8}$$

where D is the capillary diameter in inches (Green and Willhite, 1998).

Hence, the permeability of a circular opening 0.0001 in. in diameter is 0.20 Darcys or 200 mD. The permeability of a circular opening 0.01 in. in diameter is 2,000 Darcys or 2,000,000 mD.

Average permeability from a channel-matrix system can be obtained from the relationship:

$$k_{av} A = k_b (A - N\pi r^2) + k_v N\pi r^2 \tag{9}$$

where k_{av} is the average permeability, in Darcys, A is the cross sectional area, in in^2, k_b is the matrix permeability, in Darcys, k_v is the channel permeability, in Darcys, N is the number of channels per section, and r is the channel radius, in inches (Beaumont and Foster, 1987).

2.3.3 Wettability

Wettability is defined as the tendency of one fluid to spread on, or adhere to, a solid surface in the presence of other immiscible fluids. When two immiscible phases are placed in contact with a solid surface, one phase is usually attracted to the solid more strongly than the other phase. The more strongly attracted phase is called the wetting phase. For example, for the water-oil-solid system at equilibrium, the following equation (known as Young's equation) can be expressed:

$$\sigma_{os} - \sigma_{ws} = \sigma_{ow} \cos\theta \qquad (10)$$

where σ_{os} is the interfacial tension between the oil and solid, σ_{ws} between the water and solid, σ_{ow} between the oil and water and θ is contact angle measured through the water phase as show in Figure 2.1 (Torsæter and Abtahi, 1996).

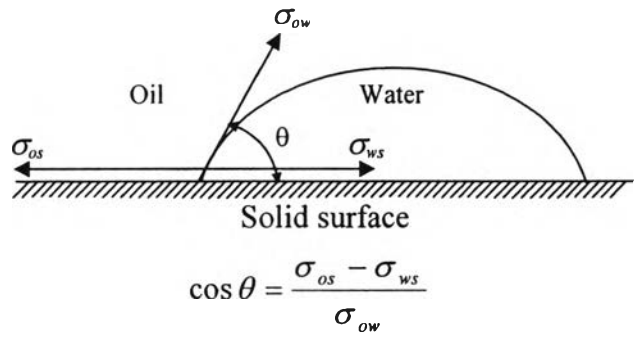

Figure 2.1 Interfacial tensions for water-oil-solid system at equilibrium (Dawe, 2000)

Based on the contact angle, the Wetting Index (WI) is defined according to Table 2.2.

Table 2.2 Wetting Index indicated by contact angle (Torsæter and Abtahi, 1996).

Wetting Index, cosθ	**Contact angle, θ**	**Wetting condition**
1.0	0°	Completely water wet, preferential wettability to water
0	90°	Neutral system
-1.0	180°	Preferential wettability to oil, completely oil wet

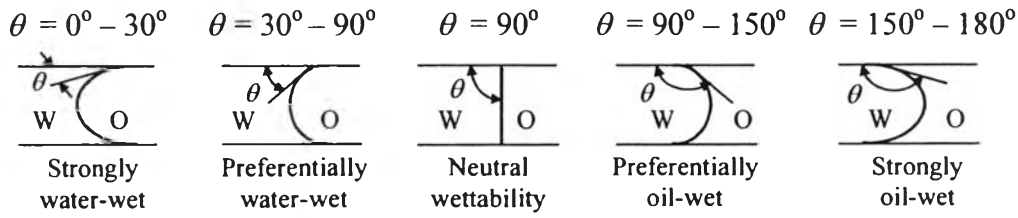

Figure 2.2 Contact angle for water-oil-solid system (Romero-Zerón, 2004)

In a rock-oil-brine system, wettability is a measure of the preference that the rock has for either oil or water. When the rock is water-wet, there is a tendency for water to occupy the small pores and to contact the majority of the rock surface (Figure 2.3(a)). In an oil-wet system, the location of the two fluids is reversed, and oil will occupy the small pores and contact the majority of the rock surface (Figure 2.3(b)) (Dawe, 2000).

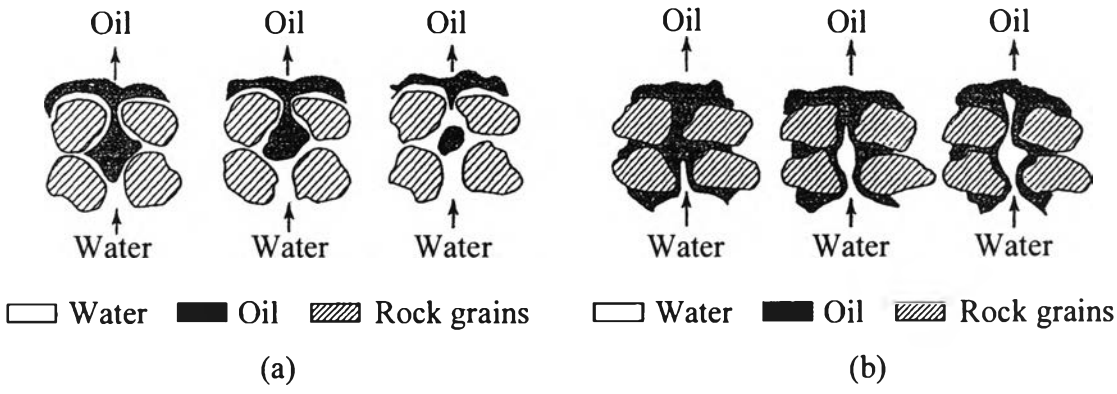

Figure 2.3 Microscopic fluid distribution for (a) water-wet and (b) oil-wet system (Dawe, 2000)

Rock wettability affects not only the nature of fluid saturations but also the general relative permeability characteristics of a fluid/rock system. Considering the effect of wettability on fluid distributions, it is easy to rationalize that relative permeability curves are strong functions of wettability (Green and Willhite, 1998).

Depending on the specific interaction of rock, oil and brine, the wettability of a system can range from water-wet, to intermediate wettability, mixed wettability and oil-wet. Intermediate wettability means that the rock has no overall preference for either oil or water. Mixed-wet means that certain parts of the interconnected pore space are water-wet, while the remaining surfaces (usually the large and interconnected pores) are oil-wet (Dawe, 2000). Because of this mixed chemical exposure, the wettability condition may vary from point to point. In fact, water sometimes wets the solid over part of the surface and oil over the remaining part (Green and Willhite, 1998).

Reservoirs can have various wettability characteristics depending on the oil composition, rock mineralogy, formation brine and its pH, pressure and temperature, and the thickness of the connate water layer i.e. the relative height above free water level (Dawe, 2000).

2.3.4 Capillary Pressure Characteristics

Capillary pressure (P_c) is the most basic rock-fluid characteristic in multi-phase flows, which reflects the interaction of rock and fluids, and therefore it is controlled by the pore geometry, interfacial tension, and wettability (Lake, 1989). By a simple model of fluid rise in a capillary tube, the capillary pressure can be illustrated as shown in Figure 2.4. The analogy is usually performed as water rise in a glass capillary. The fluid above the water is an oil, and because the water preferentially wets the glass of the capillary, there is a capillary rise (Green and Willhite, 1998).

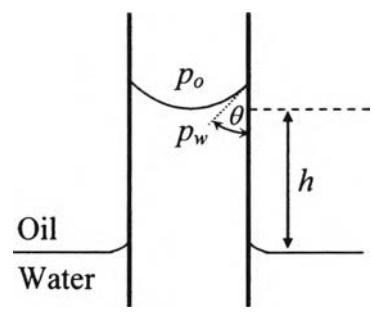

Figure 2.4 Capillary pressure resulting from interfacial forces in a capillary tube (Green and Willhite, 1998)

The water will rise in the capillary tube until it reaches a height, h, above the level interface, when capillary-gravity (hydrostatic) equilibrium is achieved. Two pressures, p_o and p_w, are the oil and water pressures on the opposite sides of the curved interface, respectively (Dake, 2002). A force balance indicates that capillary pressure, P_c, in this system is given by:

$$P_c = p_o - p_w = (\rho_w - \rho_o)gh \qquad (11)$$

The result indicates that a pressure difference exists across the interface, which is designated the capillary pressure, P_c. Note that the larger pressure exists in the nonwetting phase (Green and Willhite, 1998).

At static conditions, the force owing to surface tension (vertical component of surface tension multiplied by the wetted perimeter) will be balanced by the force of gravity acting on the column of fluid. This leads to a result of σ_{ow} for capillary rise:

$$\sigma_{ow} = \frac{rgh(\rho_w - \rho_o)}{2\cos\theta} \tag{12}$$

From Eq. (11) and (12), there results:

$$P_c = \frac{2\sigma_{ow}\cos\theta}{r} \tag{13}$$

where P_c is the capillary pressure, σ_{ow} is the interfacial tension between the oil and water, θ is contact angle between water and capillary tube, and r is the capillary tube radius (Green and Willhite, 1998).

The capillary pressure is thus related to the fluid/fluid interfacial tension, the relative wettability of the fluids (through θ), and the size of the capillary, r. The capillary pressure may be either positive or negative; the sign merely expresses in which phase the pressure is lower. The phase with the lower pressure will always be the phase that preferentially wets the capillary. Notice that P_c varies inversely as a function of the capillary radius and increases with the affinity of the wetting phase for the rock surface (Green and Willhite, 1998).

When two immiscible fluids are in contact in the interstices of a porous medium, a discontinuity in pressure exists across the interface separating them. Capillary pressure is defined as the pressure difference across a curved interface between two immiscible fluids, which is the pressure in the nonwetting phase minus the pressure in the wetting phase ($P_c = p_{nonwetting} - p_{wetting}$). In the static condition, a higher pressure is required in the nonwetting phase than in the wetting phase to keep the interface from moving (Lake, 1989). For an oil-water, gas-water or gas-oil system,

capillary pressure is defined as $P_c = p_o - p_w$, $P_c = p_g - p_w$, and $P_c = p_g - p_o$, respectively (Torsæter and Abtahi, 1996).

The general expression for calculating the capillary pressure at any point on an interface between oil and water is given by the Laplace equation:

$$P_c = p_o - p_w = \sigma_{ow}\left(\frac{1}{r_1} + \frac{1}{r_2}\right) \tag{14}$$

where σ_{ow} is interfacial tension between the oil and water, r_1, r_2 are principal radii of curvature at any point on the interface where the pressures in the oil and water are p_o and p_w, respectively (Dake, 2002).

In a straight capillary tube, $1/r_1$ and $1/r_2$ are equal and are given by the radius of the capillary divided by the cosine of the contact angle, $r/\cos\theta$. For the unconsolidated uniform spheres as shown in Figure 2.5, the values of r_1 and r_2 are related to the saturation of the wetting-phase fluid within a porous medium (Green and Willhite, 1998).

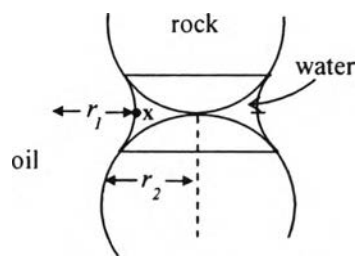

Figure 2.5 Water entrapments between two spherical sand grains in a water-wet reservoir (Dake, 2002)

In applying Laplace equation is to calculate the capillary pressure difference at a point on the interface, there is also a sign convention that the radii are positive when measured through the oil phase (r_1) and negative when measured through the water phase (r_2), in a water-wet system. Since $r_1 < r_2$, however, the capillary pressure is positive. As is evident from Figure 2.5, the volume of water (water saturation, S_w) decreases, the radii decrease, and therefore there must be some inverse relationship between P_c and S_w (Dake, 2002). This relationship is called the capillary pressure

curve, which is a function of pore sizes, wettability, interfacial tension and fluid saturation history (drainage and imbibition) (Torsæter and Abtahi, 1996).

The two dynamic situations shown in Figure 2.6 are described as (a) Imbibition; in which the wetting phase saturation is increasing and (b) Drainage; in which the wetting phase saturation is decreasing. It has been determined experimentally that the contact angle is larger when the wetting phase is advancing over the rock face than when retreating and this difference is described as the hysteresis of the contact angle. The displacement of oil by water in a water-wet reservoir is, therefore, an imbibition process. Conversely, the displacement of oil by water in an oil-wet reservoir would be a drainage process (Dake, 2002).

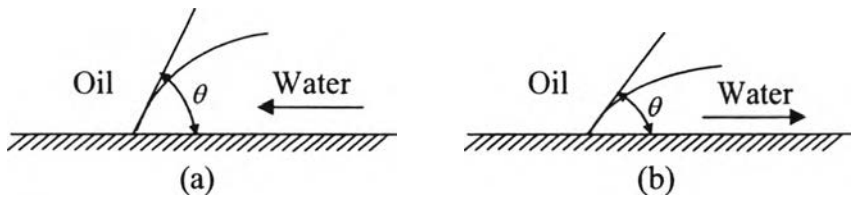

Figure 2.6 Hysteresis in contact angle in a water-wet reservoir
(a) Imbibition and (b) Drainage (Dake, 2002)

Figure 2.7 shows the drainage and imbibition curves for a water-wet reservoir. A minimum threshold pressure must be exceeded in order for the largest pore space to be penetrated by the nonwetting phase. As pressure increases further, the wetting phase saturation decreases until an irreducible wetting phase saturation (S_{wirr}) is reached in the drainage curve. The wetting phase is introduced back into the system following the imbibition curve until the wetting phase saturation has risen to its maximum value $S_w = 1 - S_{nwr}$. At this point, the capillary pressure is zero and the nonwetting phase residual saturation (S_{nwr}) is entrapped. A hysteresis effect in contact angle is observed that indicates different fluid paths and fluid distributions between drainage and imbibition. Primary drainage represents on accumulation of oil and the onset of initial reservoir conditions. Imbibition represents the displacement or production of oil upon water injection (Dawe, 2000).

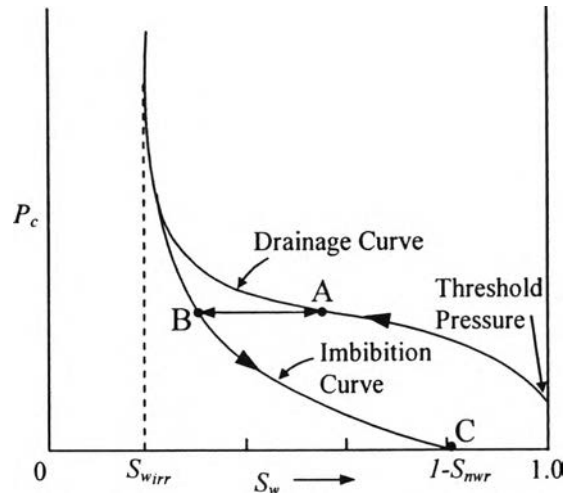

Figure 2.7 Capillary pressure curves for a water-wet reservoir (Green and Willhite, 1998)

A real permeable medium has many assemblages, like the toroid, that differ in size, and internal geometry. Consider the porous medium idealized by the arrangement of decreasing size pores, as shown in Figure 2.8. The three configurations of A, B, and C are represented in capillary pressure curves by point A, B, and C in Figure 2.7. Points A and B have equal capillary pressure but on the drainage curve and imbibition curve, respectively. The difference between the wetting phase saturation of points A and B is the disconnected nonwetting phase saturation at point B. The connected nonwetting phase configuration is identical in configurations A and B; hence the trapped nonwetting phase saturation corresponding to an initial saturation at point A is the difference between the nonwetting phase saturation at point C minus the difference between the nonwetting phase saturations at points B and A (i.e., C-[B-A]) (Lake, 1989).

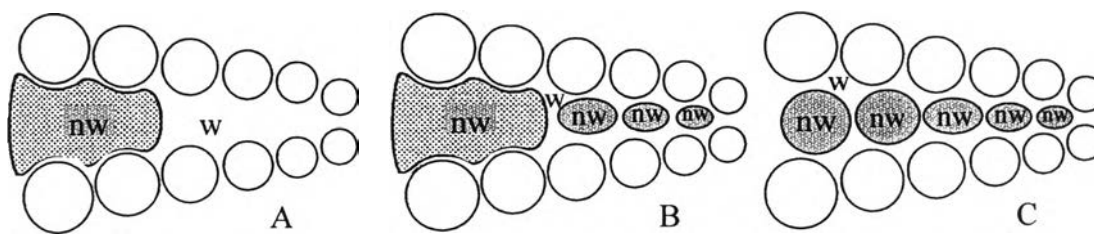

Figure 2.8 The idealized porous medium with decreasing size pores (Lake, 1989)

Since the nonwetting phase residual saturation (S_{nwr}) depends on the initial nonwetting phase saturation (S_{nwi}), this procedure yields one point on the initial-residual (IR) curve as shown in Figure 2.9. However, the whole curve may be traced by picking several points along the two P_c curves. Alternatively, if one capillary pressure curve is given along with the IR curve, the other capillary pressure curve may be estimated by the reverse procedure (Lake, 1989).

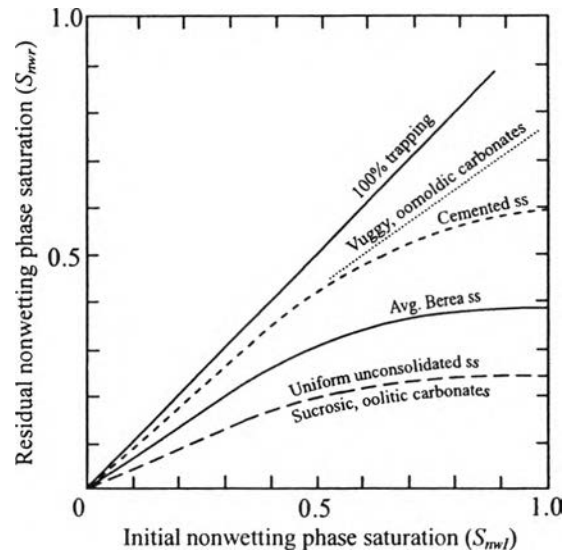

Figure 2.9 Typical IR nonwetting phase saturation curves (Lake, 1989)

2.4 Mobility Ratio

Mobility of a fluid phase flowing in a porous medium is defined on the basis of the Darcy equation:

$$u_i = -(k_i / \mu_i)(dp / dx) \qquad (15)$$

where u_i is superficial velocity of Phase i, k_i is effective permeability of Phase i, μ_i is viscosity of Phase i, p is pressure, and x is length.

For single-phase flow, k_i is the absolute permeability of the porous medium. For multiphase flow, it is the effective permeability of the flowing phase and is, therefore, a function of the saturation of the phase. Mobility of the phase, λ_i, is given by:

$$\lambda_i = (k_i / \mu_i) \tag{16}$$

In calculations involving a displacement process, a useful concept is the mobility ratio, M, of the displacing and displaced fluid phases:

$$M = \lambda_D / \lambda_d \tag{17}$$

where λ_D is mobility of the displacing fluid phase and λ_d is mobility of the displaced fluid phase. Note that M is a dimensionless quantity (Green and Willhite, 1998).

The mobility ratio is an important parameter in any displacement process. This ratio affects the stability of a displacement process, with flow becoming unstable (non-uniform displacement front) when $M > 1$. This unstable flow is called viscous fingering. Because a value of M relative to unity is so significant, a value $M > 1$ is referred to as an unfavorable mobility ratio. Conversely, a value $M \leq 1$ is a favorable mobility ratio (Green and Willhite, 1998). Further, the volumetric sweep efficiency generally increases as M is reduced, and it is sometimes advantageous to operate at a mobility ratio considerably less than unity, especially in reservoirs with substantial variation in the vertical or areal permeability (Dake, 2002).

The mobility ratio can be modified by any combination of changes in the permeabilities of the rock to the displacing and displaced fluids and/or changes in fluid viscosities:

$$M = \left(\frac{k_{rD}}{\mu_D}\right)_{S_D} \left(\frac{\mu_d}{k_{rd}}\right)_{S_d} \tag{18}$$

where k_{rD} is relative permeability in the displacing phase, k_{rd} is relative permeability in the displaced phase, μ_D is viscosity of the displacing phase, μ_d is viscosity of the displaced phase, S_D is an average saturation of the displacing phase in the region behind the displacing-phase front, S_d is an average saturation of the displaced phase in the region ahead of the displacing-phase front. Consistent units must be used (Green and Willhite, 1998).

The basic mechanics of oil displacement by water can be illustrated as shown in Figure 2.10 for both an ideal and non-ideal linear horizontal waterflood.

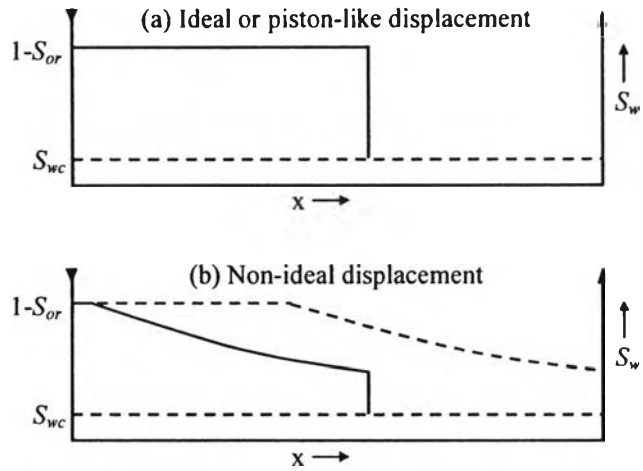

Figure 2.10 Water saturation distribution as a function of distance between injection and production wells
(a) Ideal or piston-like displacement (b) Non-ideal displacement (Dake, 2002).

In the ideal case as shown in Figure 2.10 (a), there is a sharp interface between the oil and water. Ahead of this oil is flowing in the presence of connate water, while behind the interface water alone is flowing in the presence of residual oil. This favorable type of displacement will only occur if $M \leq 1$ which means under an imposed pressure differential, the oil is capable of traveling with a velocity equal to, or greater than, that of the water. Since it is the water which is pushing the oil, there is no tendency for the oil to be by-passed which results in a sharp interface between the fluids. This ideal displacement is called "piston-like displacement". Its most attractive feature is that the total amount of oil that can be recovered from a linear reservoir block will be obtained by the injection of the same volume of water (Dake, 2002).

The non-ideal displacement as presented in Figure 2.10 (b), which unfortunately is more common in nature, occurs when $M > 1$. In this case, the water is capable of traveling faster than the oil and, as the water pushes the oil through the reservoir, the latter will be by-passed. Water fingering develops leading to the unfavorable water saturation profile. Ahead of the water front, oil is again flowing in the presence of connate water. This is followed by a waterflood front or shock front, in which there is a discontinuity in the water saturation. Then, there is a gradual transi-

tion between the shock front saturation and the maximum saturation, $S_w = 1 - S_{or}$. The dashed line in Figure 2.10 (b) depicts the saturation distribution at the time when the shock front breaks through into the producing well (breakthrough). In contrast to the piston-like displacement, not all of the movable oil will have been recovered at this time. As more water is injected, the plane of maximum water saturation ($S_w = 1 - S_{or}$) will move slowly through the reservoir until it reaches the production well. Unfortunately, in typical cases it may take five or six movable oil volumes (MOV's) of injected water to displace the one MOV of oil. At a constant rate of water injection in the unfavorable case, a large quantity of water must be injected. This protracts the time scale attached to the oil recovery and reduces the recovery economics. In addition, pockets of by-passed oil are created which may never be recovered (Dake, 2002).

Since the properties of the displaced fluid when it is oil or the permeabilities of the rock to the displaced fluids are often not feasible to change, most mobility-control processes involve an addition of chemicals to the injected fluid to improve the volumetric sweep efficiency of a displacement process. These chemicals increase the apparent viscosity of the injected fluid and/or reduce the effective permeability of rock to the injected fluid. The chemicals used are primarily polymers when the injected fluid is water. Surfactants that form foams are used when the injected fluid is a gas. In many oil recovery processes, there will be more than one displacement front. For example, many EOR processes involve the injection of multiple slugs of different fluids. The flow behavior of any specific displacement front is affected not only by the mobilities of the fluids immediately ahead of and behind that front, but also by the mobilities of fluids in regions around the other fronts. For this more general case, there is no uniquely defined mobility ratio that allows prediction of such important parameters as sweep efficiency (Green and Willhite, 1998).

2.5 Phase Trapping

Trapping of oil or other fluids in porous media depends on the pore structure of the porous media, fluid/rock interactions related to wettability, and fluid/fluid interactions reflected in interfacial tension and sometimes in flow instabilities. Trap-

ping and mobilization are related to these factors in a complex way (Green and Willhite, 1998).

2.5.1 Trapping in a Single Capillary – Jamin Effect

The pressure required to force a nonwetting phase through a capillary system, such as a porous rock, can be quite high. This phenomenon, called the Jamin effect, can be described most easily by analyzing a trapped oil droplet or gas bubble in a preferentially water-wet capillary, as shown in Figure 2.11.

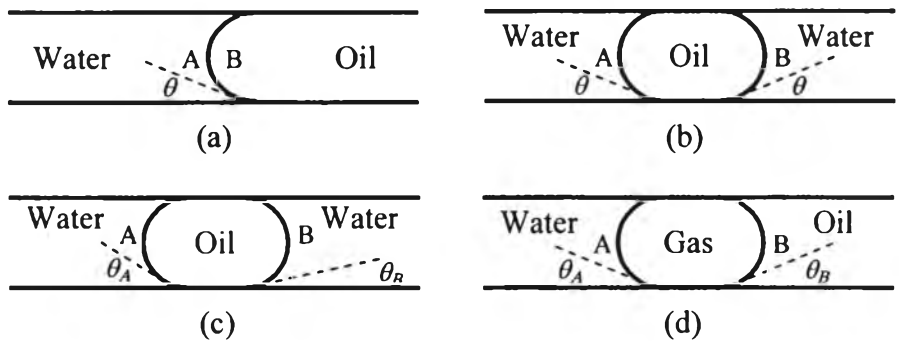

Figure 2.11 Different conditions of trapping in capillary
(a) Continuous phases (b) Oil trapped drop (c) Variation in θ (d) Variation in σ
(Green and Willhite, 1998)

Figure 2.11 (a) shows a very long, continuous water filament in contact with a continuous oil filament. The system is static, with pressure differences existing at Points A and B because of capillary forces. The static pressure difference must be exceeded for flow to occur. The pressure across the interface is the capillary pressure, P_c.

$$p_B - p_A = P_c = \frac{2\sigma_{ow}\cos\theta}{r} \tag{19}$$

Subscripts A and B indicate that the values are determined for the interfaces at Points A and B, respectively. For the finite drop in contact with immiscible fluids on both sides of the drop as shown in Figure 2.11 (b) through (d), a generalized expression can be written by simply adding pressure drops across each interface. An assumption is that the pressure within the oil or gas drop is constant from one end of

the drop to the other. Again the static pressure difference between Points A and B is important because this value must be exceeded to initiate flow (Green and Willhite, 1998).

In Figure 2.11 (b), water contacts both sides of a finite oil drop. The static pressure difference, $p_B - p_A$, is expressed as:

$$p_B - p_A = \left(\frac{2\sigma_{ow}\cos\theta}{r}\right)_A - \left(\frac{2\sigma_{ow}\cos\theta}{r}\right)_B = 0 \qquad (20)$$

Since the conditions at Point A are the same as at Point B, there would be no net pressure change across the drop. Pressure in the oil phase would exceed the pressure in the water phase by the value of P_c (Green and Willhite, 1998).

Figure 2.11 (c) presents a variation of the second case, Figure 2.11 (b), where the contact angle is different on the two sides of the drop. If the drop were displaced in one direction, causing an advancing contact angle different from a receding angle. According to Figure 2.11 (c), the advancing contact angle at Point B is smaller than a receding angle at Point A, $\theta_B < \theta_A$, and $\cos\theta_B > \cos\theta_A$. This situation occurs when the drop is on the verge of moving to the right in the figure.

$$p_B - p_A = \frac{2\sigma_{ow}}{r}(\cos\theta_A - \cos\theta_B) \qquad (21)$$

Then, $p_A > p_B$ and a pressure gradient exists in the potential direction of flow at static, or trapped, conditions (Green and Willhite, 1998).

In Figure 2.11 (d), a gas drop is trapped between water on one side and oil on the other side. Interfacial tension and contact angles are different at the two interfaces because the fluid systems are different. If $\sigma_{go}\cos\theta_B > \sigma_{gw}\cos\theta_A$, a pressure drop exists from point A to B when this system is static.

$$p_B - p_A = \frac{2}{r}(\sigma_{gw}\cos\theta_A - \sigma_{go}\cos\theta_B) \qquad (22)$$

For any situations in Figure 2.11, if the parameters are known or can be estimated, the pressure drop required to initiate flow can be calculated (Green and Willhite, 1998).

2.5.2 Trapping in a Single Capillary with Fluid Bypassing

Pore channels in reservoir rocks are not straight, smooth capillaries but irregularly shaped channels. Isolated oil drops in a channel do not ordinarily seal the channel; bypassing by a second phase is possible because of channel geometry. The calculations of the Jamin effect in the previous section assumed static conditions with no bypassing of oil drops by the water phase. The force balance indicates that the oil drop will be trapped since capillary forces are balanced by viscous forces in the flowing water. Viscous forces consist of form drag (resulting from the channel geometry) and interfacial shear (Green and Willhite, 1998).

2.6 Polymer Flooding

Polymer applications in oilfields are used to improve volumetric sweep efficiency of the reservoir. Polymer solutions are designed to develop a favorable mobility ratio (decreasing the mobility). Polymers which dissolve in an aqueous solution help to increase the viscosity of the aqueous solution, as well as decrease the permeability of the porous media that occurs with some polymers. Polymer Flooding is normally applied when either of the following situations occurs: 1) the waterflood mobility ratio is high or 2) the heterogeneity of the reservoir is high (Lake, 1989).

2.6.1 Polymer Types

There are two different types of water-soluble and viscosity-enhancing polymer chemistries that have been used during polymer flooding. The first type is biopolymers which are polysaccharides (poly sugars) such as Xanthan gum polymer. The second type is synthetic polymers such as acrylamide-based polymers. Polyacrylamides (PAM), a type of synthetic polymers, have an acrylamide molecule as a monomeric unit. Pendant water-soluble chemical groups on the molecule (i.e. amide groups) render the polymer molecule to be soluble in water (Sydansk, 2005). As used in polymer flooding, polyacrylamides have undergone partial hydrolysis, which causes anionic carboxyl groups ($—COO^-$) to be scattered along the backbone chain. These polymers are called partially hydrolyzed polyacrylamides (HPAM). Figure

2.12 shows the molecular structures of PAM and HPAM, when x and y are the amount of monomeric units in one polymer chain (Lake, 1989).

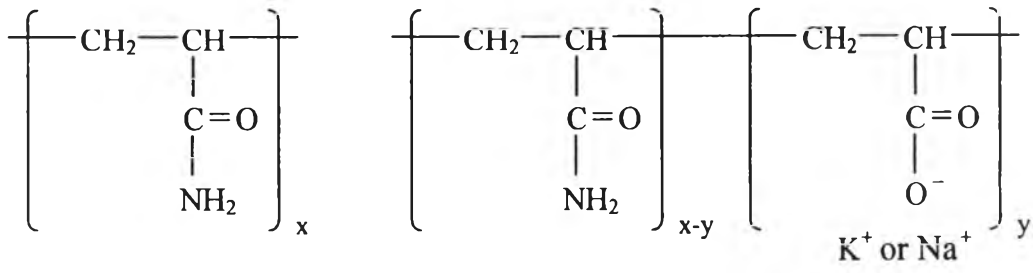

Figure 2.12 Molecular structures of PAM and HPAM (Lake, 1989)

In the relatively low salinity brine, PAM is not as good a viscosity-enhancing agent and is not propagated as well through sand reservoirs compared to HPAM. Since PAM is slightly cationic in an acidic or neutral pH environment, it tends to adsorb onto reservoir rock surfaces, especially sands and sandstone pore surfaces. For these reasons, HPAM is most often favored for use in polymer flooding. Typical degrees of hydrolysis are 30-35 % of the acrylamide monomers. This degree of hydrolysis has been selected to optimize certain properties such as water solubility, viscosity, and retention. If hydrolysis is too small, the polymer will not be water soluble. If it is too large, its properties will be too sensitive to salinity and hardness (Lake, 1989).

2.6.2 Polymer Functions

Polymers are used in two different EOR schemes. The first scheme is increasing viscosity of the injected water with polymer. This may be beneficial when the oil being displaced in a waterflooding process is more viscous than the water, and the displacement process is less efficient than when the viscosities are more equal. Polymer flooding only affects the fluid mechanics and hence the area of the swept zone. The polymer decreases the mobility ratio, so that the flooding can lead to better sweep efficiencies than could be achieved by unviscosified water injection alone (Dawe, 2000).

The second scheme is reducing the permeability of selected volumes in the reservoir. For example, polyacrylamide polymers are adsorbed on porous media and/or are mechanically entrapped as a result of their large physical size. This polymer retention reduces the amount of polymer in solution but also causes a decrease in the effective permeability of the porous medium. The mobility of a polyacrylamide polymer solution is thus reduced to less than that of the displaced oil/water bank by a combination of increased solution viscosity and effective permeability reduction (Green and Willhite, 1998).

In addition, the major hazard to efficient oil recovery is reservoir heterogeneity, especially high permeability streaks, since the injection fluid will preferentially move through this zone and early breakthrough would occur. Conformance adjustment aims to block the zone or lower its permeability to force the displacing water to more productive areas, or simply to prevent it from being produced. Water shut-off with remedial cementing operation or cement squeezes have not proved reliable. Polymer gels formed by crosslinking can be used. In practice, the entire high-permeability area has to be blocked, otherwise, fluid readily by-passes the blocked area and goes straight back into the remaining high-permeability volume. Often, for near-wellbore treatments, small quantities of strong gel chemicals can be used to prevent water production, whereas for deeper treatments weaker gels are used to block the higher-permeability zones. New polymer systems are being developed, particularly with time-setting temperature catalytic effects (Dawe, 2000).

During polymer flooding, problems can occur within the reservoir because of adsorption, polymer slug breakdown and polymer degradation due to temperature, free radicals, pH, shear (especially extensional shear, with extensional viscosity being important) or salinity. These can be particularly severe for polymers such as polyacrylamides, polysaccharides, and xanthan gums. Storage, mixing, metering, and deoxygenating (to prevent bacterial activity) outside the reservoir are also problematic (Dawe, 2000).

2.6.3 Polymer Applications

The principal benefit of polymer solutions for use in flooding oil reservoirs is the aqueous solution's enhanced viscosity. Aqueous polymer solutions that are

used for conformance improvement flooding normally exhibit non-Newtonian viscosity properties. The viscosity of a polymer solution is indicated the resistance to flow. Common fluids, such as water and motor oils, are Newtonian fluids. The viscosity of a Newtonian fluid at a given temperature is a single value that is independent of shear rate. On the other hand, polymer solutions of the type employed in polymer flooding normally exhibit shear-thinning behavior when subjected to sufficiently high shear rates (~1 to 100 s^{-1}) but not at low shear rates (< 0.1 s^{-1}). For a shear-thinning fluid, the apparent viscosity of the fluid decreases as the fluid experiences increasing shear rates. The shear-thinning viscosity behavior of the polymer becomes relatively less pronounced as the concentration of the polymer in solution decreases. Also the viscosity at any given shear rate increases as polymer concentration increases (Sydansk, 2005).

The shear-thinning viscosity behavior of oilfield polymer solutions is favorable. When polymers flow in the far-wellbore region, and in the vast majority of the reservoir volume, the shear rate experienced by the polymer is usually quite low (about 1 to 5 s^{-1}) and is a shear rate where the polymer exhibits near maximum viscosity. In the near-wellbore region where the shear rate can be high, and when these shear rates are often in the shear thinning range for the polymer (e.g. 1 to 100 s^{-1}), the polymer shear thinning is beneficial. Because the viscosity of polymer solution is reduced, this improves the injectivity of the polymer solution (Sydansk, 2005).

Polymer flooding has been conducted successfully in 1) sandstone and carbonate matrix-rock reservoirs, 2) fractured reservoirs, and 3) water-wet mixed wetting and oil wet (Sydansk, 2005).

In a typical application, a solution of partially hydrolyzed polyacrylamide polymer in brine, at a concentration of a few hundred to several hundred ppm of polymer, is injected to displace oil (and associated water) toward production wells. The size of the polymer slug might be as much as 50 to 100 % Pore Volume (PV) and might be varied in composition. That is, the highest polymer concentration used is injected for a period of time followed by slugs at successively lower concentrations. The final fluid injected is water or brine (Green and Willhite, 1998).

Table 2.3 shows the screening criteria as to where polymer flooding is most likely applicable in terms of reservoir properties (Abou-Kassem, 1999).

Table 2.3 Screening criteria for polymer flooding (Abou-Kassem, 1999)

Parameters	Range of Values
Permeability	> 200 mD
Initial water saturation	10 – 50 %
Residual oil saturation	> 20 %
Water Salinity	< 10,000 ppm
Oil gravity	> 25 °API
Oil Viscosity	< 100 cP
Mobility Ratio	1 – 40
Temperature	< 150 °F
Drive Mechanism	No gas-cap and no bottom water drive

In 1986, a polymer flood pilot project was initiated in the Rapdan field, Saskatchewan, Canada. The pilot consists of 13 producers and 5 injectors. The average porosity and permeability were 18 % and 115 mD, respectively. The oil viscosity was 10.6 cP at the reservoir temperature of 55°C. Since an unfavorable mobility ratio of 4.5 was determined for waterflooding, which began in 1962, polymer flooding was subsequently conducted to reduce the mobility ratio by increasing μ_w (viscosity of water phase) and decreasing k_{rw} (relative permeability in the water phase). By 1994, 43 %PV (pore volume) of 21 cP polymer solution (1,100 to 1,500 ppm polyacrylamide) had been injected. The production increased from 65 m^3/d at an oil cut of 18% during 1986-87 to a peak production of 180 m^3/d at an oil cut of 36% in June, 1990. A reasonably good economic return has been achieved. The capital investment of $4 million to drill infill wells and install facilities paid out in < 5 years on the basis of an oil price of $78.63/$m^3$. Assuming a 50 %PV of polymer injection, the projected efficiency of the polymer flood would be 4.28 kg polymer/m^3 incremental oil ($18.11/$m^3$ incremental oil) (Pitts *et al.*, 1995).

2.7 Polymer Gel Treatment

When a displacement process is implemented in a reservoir with large variations in vertical permeability, injected fluid tends to flow through the zones with the highest permeabilities; thus, low-permeability zones may receive only a small fraction of the injected fluid. Bypassing part of the reservoir by the injected fluid can lead to production of relatively large volumes of injected fluid per barrel of recovered oil. The result can be that the displacement process reaches the economic limit at a time when a large volume of oil remains in the bypassed or unswept regions of the reservoir (Green and Willhite, 1998).

The objective of polymer gel treatment is treating the reservoir in a way that the effective permeability of the high-permeability zones is significantly reduced. Provisions must be made to prevent the gelling agents from entering and damaging the lower-permeability zones (Green and Willhite, 1998).

The crosslinked polymer gel is an elastic and semi-solid material that results from chemically crosslinking water-soluble polymers in an aqueous solution. By simply adding a single aqueous crosslinking-agent solution to the aqueous polymer solution, the gels are produced. Polymer and the crosslinker react to form a viscous gel i.e. a fluid with a very high apparent viscosity. The gel is essentially immobile and thus acts to reduce the apparent permeability of the rock matrix or fracture. Oilfield conformance-improvement polymer gels contain polymer concentrations in the range 150 to 100,000 ppm (most commonly 3,000 to 12,000 ppm) (Sydansk, 2005).

2.7.1 Gel Treatment Functions

Oilfield conformance gels are permeability-reducing agents. These gels work as blocking and plugging agents to fluid flow in the reservoir volume in which they have been placed. If a gel is placed some significant distance into the fractures of a naturally fractured reservoir surrounding an injection well, the gel functions also as a diverting agent. In this case, the gel will divert fluid flow from high-permeability low-oil-content fractures to low-permeability high-oil-saturation matrix reservoir rock that is adjacent to the gel-filled and gel-treated fractures. More sweep efficiency and incremental oil production results. In this type of scenario, the gel not

only functions as a blocking agent, but also functions as a diverting agent (Sydansk, 2005).

In practise, treatment tends to be limited to relatively near the wellbore in order to reduce permeability from the injection wells to production wells. The gel has been selectively placed in high-permeability strata. Such gels function purely as a plugging and blocking agent to reservoir fluid flow in the treated strata (Sydansk, 2005). Permeability modification has been applied most commonly to injection wells but also is applicable to production wells. Production well applications typically involve use of a polymer gel to shut off or to reduce water production where, for example, water coning is occurring. In this case, the gels reduce oil-production operating costs by reducing excessive, deleterious, and competing co-production of water or gas (Green and Willhite, 1998).

Gels contain large quantities of water (often produced brine in the case of oilfield gels) with the remainder of the gel constituents being low concentrations of relatively inexpensive polymers and chemical crosslinking agents. Gel conformance treatments are usually applied in the course of ongoing primary, secondary, and tertiary oil-recovery operations. Gel conformance treatments are an emerging oilfield technology that can help extend the life of maturing oil reservoirs that are approaching their economic limit and abandonment (Sydansk, 2005).

2.7.2 Cr(III)-Carboxylate/Acrylamide-Polymer (CC/AP) Gel Technology

In situ permeability-modification processes are based on the gelation of high-molecular-weight polymers such as HPAM and polysaccharides which bound together into a gel structure through the use of a crosslinking chemical agent such as trivalent cations, Cr(III) or Al(III). Cr(III)-Carboxylate/Acrylamide-Polymer (CC/AP) gel technology is widely applied and quite successful for use in oilfield conformance-control, sweep-improvement, and water/gas shutoff treatments. Cr(III) at low concentrations is relatively nontoxic to aquatic life. Cr(III) can be introduced directly as chromium acetate which is highly water-soluble and readily mixes with acrylamide-polymer solutions. This commodity chemical is readily available and relatively inexpensive. The cost of the crosslinking agent during field use has typically been 10 – 20 % of the polymer cost. Since, complexation of the Cr(III) prevents chromium

precipitation at high pH, the process is less sensitive to pH and gelation will occur at high pH. The gelation rate can be controlled to give gel times from minutes to days to weeks. For any given CC/AP gel formulation, the gelation rate increases with increasing temperature. This process is reported to produce gels at temperatures exceeding 200°F. Furthermore, the gelation is not adversely affected by H_2S (Sydansk, 1990).

There are presently two major conformance-treatment formulations of the CC/AP gel technology that are in wide usage. The first version involves the use of high molecular weight polymers (> 4,000,000) incorporated into the gels at relatively low polymer concentrations (~3,000 to 20,000 ppm). This version is usually employed to selectively treat fractures within petroleum reservoirs. These gels are often applied as relatively large volume treatments (e.g. 500 to 40,000 bbl) and are often formulated with saline produced waters. The second version of the CC/AP gel technology involves the use of relatively low molecular weight polymers (~200,000 to 2,000,000) and relatively high (~35,000 to 70,000 ppm) polymer concentrations in the gel formulations. This version of the gel technology is used in total-fluid-shutoff treatments that are usually applied in the near wellbore (often <15 ft radial penetration) region of matrix rock reservoirs. The use of fresh water within the formulations of these particular gels tends to standardize their formulations without adding substantial cost to the relatively small volume (usually <500 bbl) treatments of this near-wellbore fluid-shutoff technology (Sydansk and Southwell, 2000).

In the implementation of a treatment of this gel type, system components are mixed at the surface, usually by passing the different solutions through an in-line mixer. The gel solution is then pumped into the reservoir, where the reaction proceeds until a gel is formed. Gel slug size must be designed to be compatible with the gelation time at reservoir conditions. For this process, if the chemical system were mixed and allowed to gel at the surface before it was pumped, the shear imposed during injection would destroy the gel. Premature gelation may cause plugging of the wellbore (Green and Willhite, 1998).

2.8 Principles of Magnetic Resonance Imaging (MRI)

Magnetic Resonance Imaging (MRI) is an imaging technique that produces images of internal physical and chemical characteristics of an object from externally measured nuclear magnetic resonance (NMR) signals. NMR has existed since 1945. It is a phenomenon involving magnetic fields and radiofrequency (RF) electromagnetic radiation. Image formation using NMR signals is made possible by the spatial encoding. MRI can generate two-dimensional images at any orientation, three-dimensional volumetric images, or even four-dimensional images representing spatial-spectral distributions, as well as three-dimensional images with time dimensions (Liang and Lauterbur, 2000).

The RF range used in MRI does not involve the use of ionizing radiation and does not have the associated potential harmful effects. Energies in NMR correspond to relatively weak interactions between a nucleus and a magnetic field, in contrast to transitions in the optical or IR range, which correspond to breaking or vibrating the much stronger chemical bonds (Partain *et al.*, 1983) as shown in Figure 2.13.

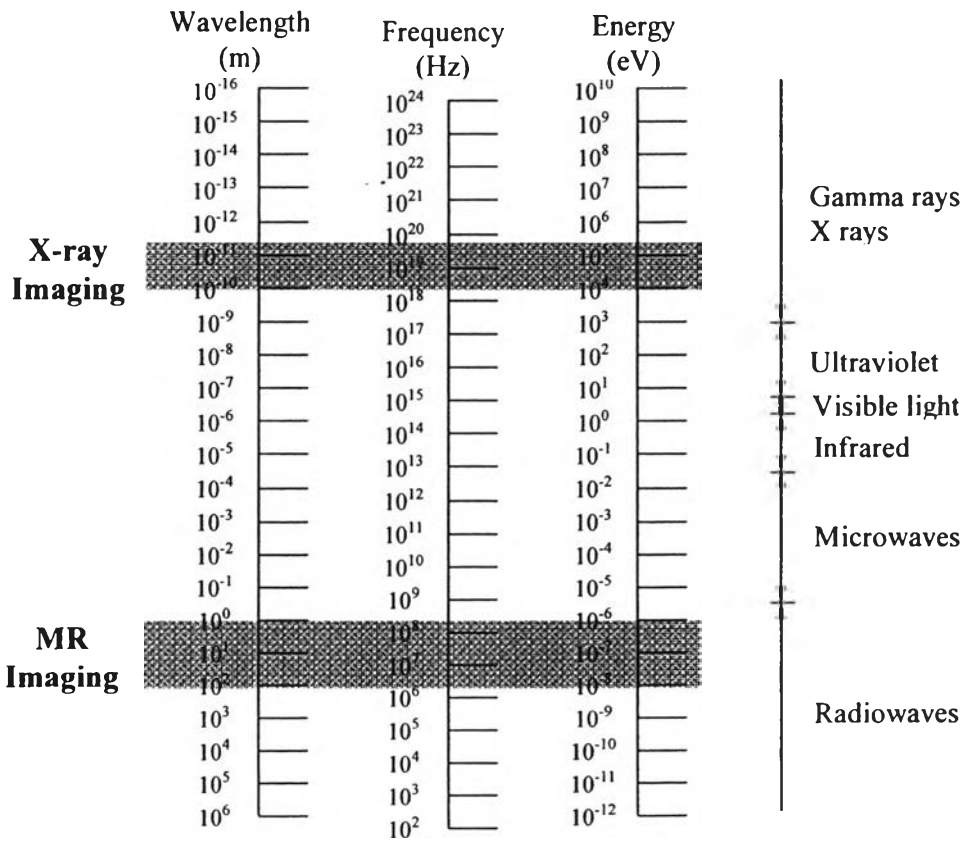

Figure 2.13 Electromagnetic spectrum (Liang and Lauterbur, 2000)

Figure 2.14 (a) illustrates the principles of MRI which can be simplified by returning to the childhood days of whip and top. The top is spun about its axis by the whip, but it also wobbles around the vertical gravitational field, particularly as it slows down. This wobbling is called a *precession*. The protons of hydrogen also behave like very tiny bar magnets of a definite strength or magnetic moment. In the absence of externally applied magnetic moments, they have no preferred orientation. However, if they are placed in a magnetic field (B_0), they will line up in one of two possible orientations: alignment parallel or anti-parallel to B_0. The spin associated with the magnetic moment causes the moment to precess around the axis of B_0. This precession defines the surface of a cone as presented in Figure 2.14 (b) (Partain *et al.*, 1983).

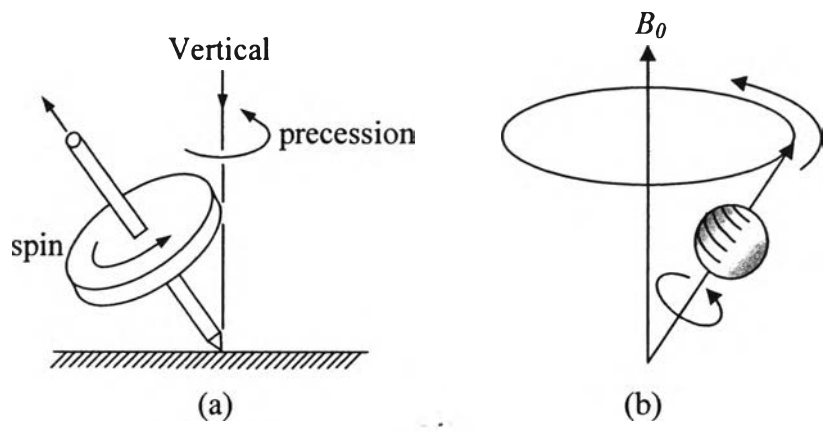

Figure 2.14 (a) A spinning top is precessing around the vertical field of gravity (b) A nucleus in the presence of an externally applied magnetic field (B_0) (Partain *et al.*, 1983)

Therefore, depending on their orientation, two groups or populations of spins can be defined. Alignment parallel to B_0 is a lower energy orientation and is thus preferred, while the anti-parallel alignment is the higher energy state as shown Figure 2.15 (a). This situation of only two allowed states is for nuclei whose "magnetic spin quantum number" is equal to ½. This includes ^{1}H, ^{13}C, ^{19}F, ^{31}P and others. From Figure 2.15 (b), each of the vectors (arrows) represents an individual spin. Since it is already known that there are more spins aligned with B_0 than against B_0, the contribution of the bottom cone cancels out, leaving only the excess spins of the

top cone to consider. Any given vector on the top cone could be described by its components perpendicular to and parallel to B_0. Clearly, for a large enough collection of spins randomly distributed on the surface of the cone, individual components perpendicular to B_0 will cancel each other. This leaves only the contributions parallel to B_0, explaining why the bulk net magnetization is indeed parallel to B_0 (Liang and Lauterbur, 2000).

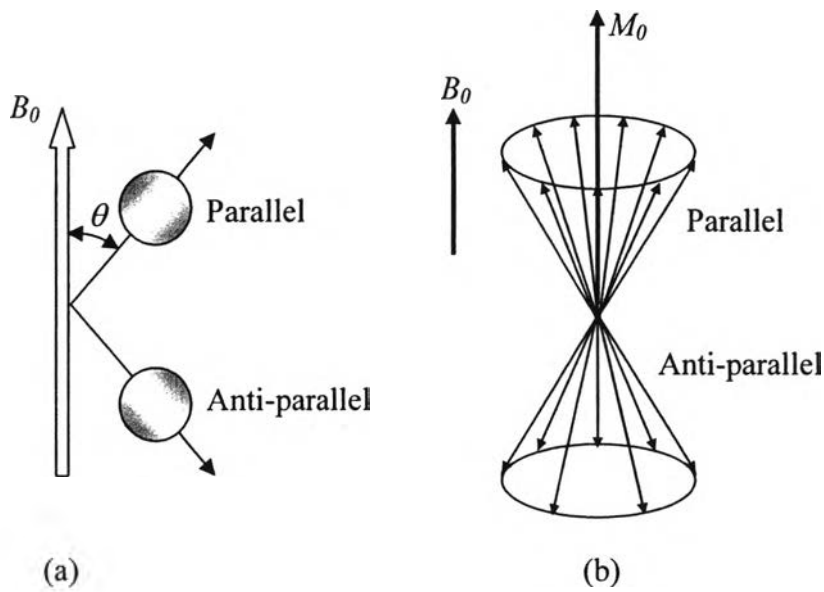

Figure 2.15 (a) Spins aligned in two orientations with respect to B_0
(b) The bulk net magnetization (M_0) results from summation of individual spins
(Liang and Lauterbur, 2000)

The interaction of a magnetic moment M_0 in the presence of a static magnetic field B_0 results in a torque, which will cause the net sample magnetization to precess about the static magnetic field. This precessional frequency is expressed by the Larmor equation:

$$\omega_0 = \gamma B_0 \qquad (23)$$

where ω_0 is the precessional frequency (Larmor frequency) in MHz, B_0 is the strength of the magnetic field in Tesla, and γ is the gyromagnetic ratio of the nucleus which is related to the strength of the magnetic moment for the type of nucleus considered. The γ values of some clinically relevant nuclei are listed in Table 2.4. For

instance, the resonant frequency for ^{1}H in a 2.4 Tesla magnet is approximately 100 MHz (Barrita, 2002).

Table 2.4 Properties of some NMR-active nuclei (Liang and Lauterbur, 2000)

Nucleus	Spin	Gyromagnetic Ratio, γ(MHz/T)
^{1}H	1/2	42.58
^{13}C	1/2	10.71
^{19}F	1/2	40.05
^{31}P	1/2	11.26

In order to detect a signal, a condition of resonance needs to be established. The system is perturbed by a radiofrequency (RF) pulse, and energy dissipation is mediated by relaxation processes. The excitation is accomplished by applying a short duration, high intensity magnetic field orthogonal to B_0 that oscillating at the Larmor frequency. This RF pulse is considered as another magnetic field, B_1, which rotates the net magnetization away from the B_0 direction. The net magnetization is rotated by a certain angle away from the longitudinal axis, this angle is termed the flip angle (α). Figure 2.16 (a) presents the situation immediately after applying a 90° pulse. The net magnetization now lies in the transverse plane and begins to precess around the B_0 axis. It yields a voltage and induces an alternating (AC) current in a coil of wire, and that current can be used to detect the action of magnetization in the transverse plane (M_{xy}) as shown in Figure 2.16 (b). The transverse magnetization decays over time, which is represented by a decreasing length of the vector (Halse, 2004).

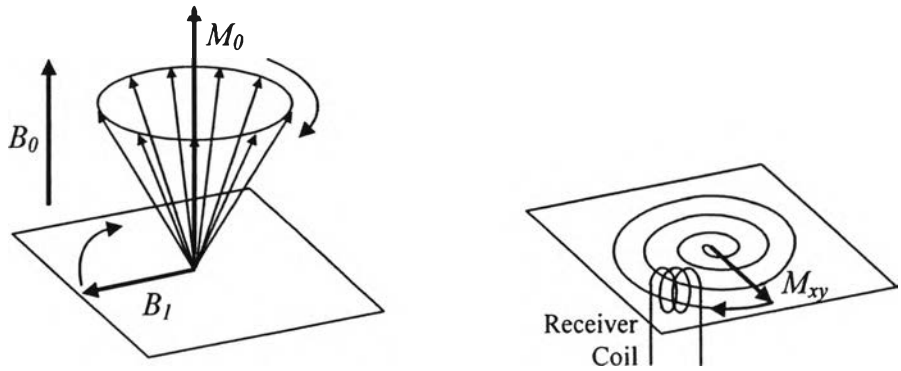

Figure 2.16 (a) RF pulse (B_1) rotates M_0 by 90°, i.e. into the transverse plane (b) The rotating magnetization induces an AC current in the receiver coil (Barrita, 2002)

The time dependent signal recorded by the receiver coil is called the free induction decay (FID). It is so-called because the signal is not driven by the presence of the B_1 field (RF pulse) at the time of observation. The signal induced in the receiver coil gets weaker with time. The signal decay is due to a process known as relaxation as shown in Figure 2.17. In practice, the same RF coil used for excitation is used for detection of the NMR signal (Halse, 2004).

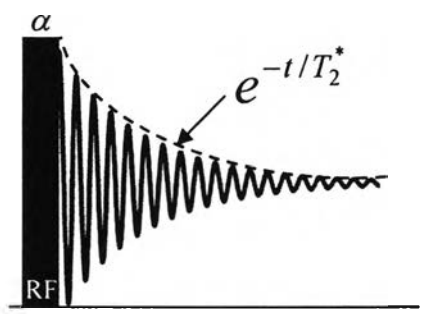

Figure 2.17 Free induction decay (FID) is characterized by the time constant T_2^* (Halse, 2004)

2.8.1 Relaxation

After the spin system is perturbed, the excited spins return to their equilibrium energy level and orientation. This is called relaxation. The relaxation process

can be divided into the transverse plane independent of the relaxation along the longitudinal axis (Barrita, 2002).

2.8.1.1 Transverse Relaxation

As shown in Figure 2.17, the transverse magnetization decays exponentially to zero. The relationship describing the decay is:

$$M_{xy} = M_{xy}^{0}\, e^{-t/T_2^*} \tag{24}$$

where M_{xy}^{0} is the initial amount of transverse magnetization, M_{xy} is the amount of transverse magnetization at any given time (t) after a pulse, and T_2^* is the effective spin-spin relaxation time which characterizes the rate of decay (Barrita, 2002).

In the case of $t = T_2^*$, hence $M_{xy}(T_2^*) = 0.37\, M_{xy}^{0}$. This means T_2^* is the time that transverse magnetization decays to 37% of the initial value.

The decay occurs when transverse magnetization is caused by "dephasing" which different components of the magnetization precess at slightly different rates. Since the signal recorded is the sum of all the transverse components, sufficient dephasing will lead to complete cancellation of the signal. There are two factors that contribute to the decay of transverse magnetization – spin interactions and B_0 inhomogeneity (Chen *et al.*, 2006).

A loss of phase coherence within the spin system due to the interactions between neighboring spins is called spin-spin relaxation (T_2 relaxation). It is a function of the sample as well as the static field strength, B_0. The decay of the transverse component of the net magnetization, M_{xy}, is given by:

$$M_{xy} = M_{xy}^{0}\, e^{-t/T_2} \tag{25}$$

B_0 inhomogeneity or field variation induced by the sample itself can add to the loss of coherence and hence the decay of the transverse magnetization. T_2^* is defined by Eq. (26), where ΔB_0 represents the local or bulk magnetic field inhomogeneity:

$$\frac{1}{T_2^*} = \frac{1}{T_2} + \gamma \Delta B_0 \tag{26}$$

A "spin echo" is created from a series of RF pulses as shown in Figure 2.18. A spin echo is generated by the application of an initial 90° RF pulse, then after a time delay (*TE*/2), an 180° RF pulse is applied. The peak of the first echo occurs at the echo time (*TE*) after the initial 90° pulse. Further echoes are obtainable with additional 180° pulses. Notice the decay envelope of the echo maxima, governed by T_2, and the characteristic time with which each echo forms and decays, T_2^* (Barrita, 2002).

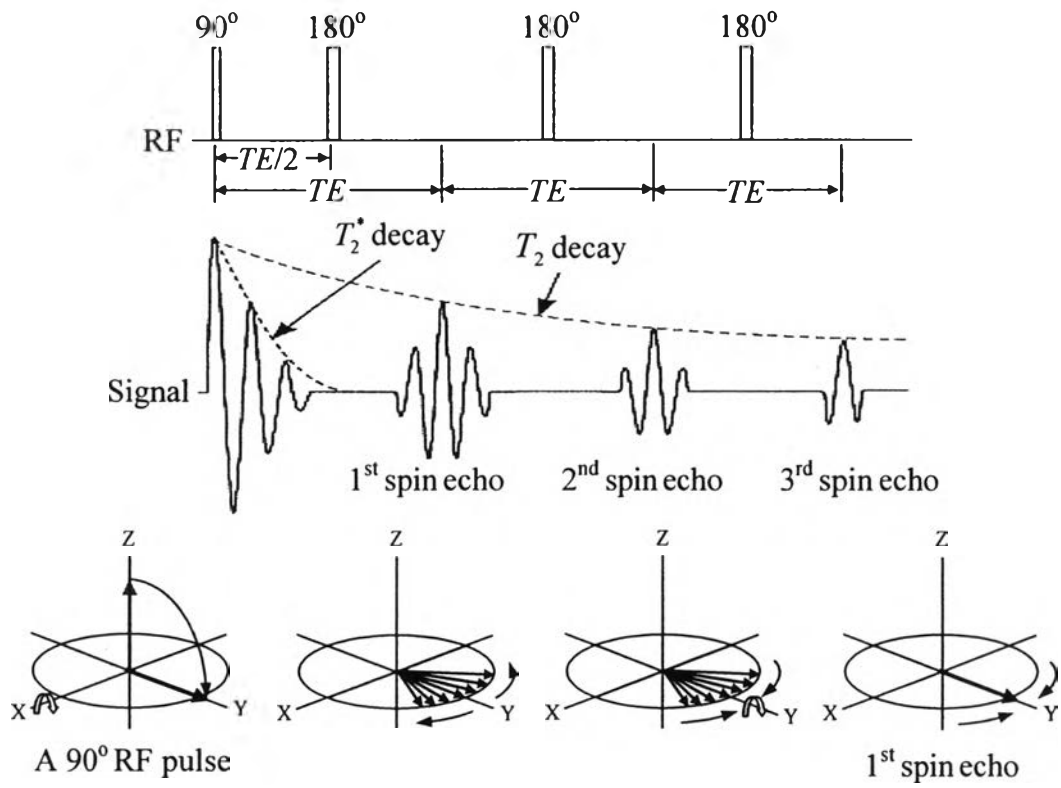

Figure 2.18 Spin echo (Halse, 2004)

2.8.1.2 Longitudinal Relaxation

The exponential recovery of longitudinal magnetization, M_z, after an excitation pulse along the B_0 direction is know as spin-lattice relaxation (T_1 relaxation). Longitudinal relaxation restores the original equilibrium population difference by returning some spins to the lower energy state, and in the process giving up thermal

energy to the environment (lattice). Longitudinal magnetization builds up from zero to a maximum which can be expressed by the following equation:

$$M_z = M_0\left(1-e^{-t/T_1}\right) + M_z^0 e^{-t/T_1} \qquad (27)$$

where M_z^0 is the initial amount of longitudinal magnetization, M_z is the amount of longitudinal magnetization at any given time (t) after a pulse, and T_1 is the spin-lattice relaxation time (Liang and Lauterbur, 2000).

From the above equation, M_z will regain 63% of its thermal equilibrium value after a time interval T_1. This statement implies the rate of increase in longitudinal magnetization is fastest when M_z is very far from its equilibrium value and it is considered that full recovery is achieved after 5 times T_1 (Barrita, 2002).

2.8.2 Spatial Encoding and Image Field of View (FOV)

The main idea of MRI from the starting point until getting the images is shown below:

$$\vec{\mu} \rightarrow \vec{M}_0 \rightarrow \vec{M}_{xy} \rightarrow S(t) \rightarrow S(\vec{k}) \rightarrow I(\vec{x}) \qquad (28)$$

First, one starts with the microscopic magnetic moments $\vec{\mu}$ in an object and then trace step-by-step how they are subsequently converted to a bulk magnetization $\vec{M}_0$, a transverse magnetization $\vec{M}_{xy}$, an electrical signal $S(t)$, a k-space signal $S(\vec{k})$, and finally the desired image $I(\vec{x})$ (Liang and Lauterbur, 2000).

$\vec{\mu} \rightarrow \vec{M}_0$ is accomplished by exposing the object to the B_0 field; $\vec{M}_0 \rightarrow \vec{M}_{xy}$ is done with RF excitations; $\vec{M}_{xy} \rightarrow S(t)$ is known as signal detection based on Faraday's law of induction; $S(t) \rightarrow S(\vec{k})$ is the heart of MRI, and involves the use of magnetic field gradients to encode spatial information into the transient responses of a spin system upon RF excitations. Finally $S(\vec{k}) \rightarrow I(\vec{x})$ is the well-known image reconstruction problem common to many tomographic imaging modalities (Liang and Lauterbur, 2000).

The principle behind magnetic resonance imaging is the Larmor equation, which states the dependence of the frequency on the magnetic field. This equation suggests that by manipulating the magnetic field, it is possible to encode the NMR signal with position information. That is, the acquired signal contains information about the relative locations of the spins in the sample. This spatial information is acquired through the use of the magnetic field gradient. For example, the linear magnetic field gradients G (Gauss/cm) are used to encode position information within the detected signal. The use of magnetic field gradients in three orthogonal directions makes it possible to label each unit volume in space (voxel), with its own frequency, as indicated by the following equation (Barrita, 2002):

$$\omega_0 (x) = \gamma (B_0 + G_x x) \tag{29}$$

Encoding the position of the detected signal is usually achieved through encoding position information into either frequency or phase. Since the k-space encoding vector is defined as a function of both gradient field strength and time, in the frequency encoding methods, the k-space vector is sampled as a function of time. The simplest implementation of this approach is to excite the signal with an RF pulse and then sample the resultant FID as a function of time. This approach presents a few immediate limitations. First, due to hardware constraints, such as the finite gradient rise times and dead times between transmission of the RF excitation and collection of the MR signal, the time point $t = 0$ can not be sampled and hence the centre of k-space is not sampled directly. Secondly, negative time points can not be sampled. To solve these problems, the "spin echo" technique is applied. As explained in the previous section according to Figure 2.18, a 90° RF excitation pulse is applied to fully rotate the net magnetization into the transverse plane. In this case the z magnetization is transformed into y magnetization. Second, the phases of the spins evolve in the presence of a magnetic field gradient. During this time, the spins precess at frequencies which are a function of position and thus a de-phasing about the y-axis is observed in the rotating frame. At a time $TE/2$ following the original excitation, an 180° RF pulse is applied to reverse the orientation of the spins about the y-axis. During the subsequent phase evolution period, the spins will re-phase and refocus at a time TE.

This refocused signal is known as a spin echo. The echo centre, corresponding to the centre of *k*-space, is at *TE* (Barrita, 2002).

In phase encoding techniques, the *k*-space vector is sampled as a function of gradient field strength. Following RF excitation and under the influence of a constant magnetic field gradient $\vec{G}$, the spin system evolves for a fixed period of time. During this evolution time, each spin acquires a phase which is directly correlated with its spatial position. At a fixed time, called the encoding time t_p, in pure-phase encode methodologies, a *k*-space datum point is acquired. This *k*-space point is characterized by the gradient field strength and the encoding time. Subsequent *k*-space points are acquired with different gradient values but with the same encoding time. In this manner, the sampling of the *k*-space vector is a function of $\vec{G}$ not *t* (Halse, 2004).

The spatial extent of an image is called the image field of view (FOV) and is calculated as the inverse of the *k*-space step size. An image FOV can be computed for both frequency encoding and phase encoding methods:

$$\mathrm{FOV}_{\mathrm{freq}} = \frac{1}{\Delta k_x} = \frac{2\pi}{\gamma G_x \Delta t} \tag{30}$$

$$\mathrm{FOV}_{\mathrm{phase}} = \frac{1}{\Delta k_x} = \frac{2\pi}{\gamma \Delta G_x t_p} \tag{31}$$

The fields of view calculated above are one dimensional, arbitrarily chosen as the *x* dimension, but the same form holds for all dimensions. Notice that, the FOV for frequency encoding is determined by the gradient field strength and the dwell time, Δt, between sampled points, whereas the FOV for the phase encoding is determined by the encoding time t_p and the gradient step size (Halse, 2004).

2.8.3 Centric Scan SPRITE MRI Technique

The Centric Scan SPRITE (Single Point Ramped Imaging with T_1-Enhancement) MRI is a pure phase encoding technique that has proven to be a very robust and flexible method for the study of a wide range of systems with short signal lifetimes such as porous media. The traditional spin echo MRI methods which are based on frequency encoding MRI techniques suffer from image distortion due to

susceptibility variations, chemical shift and paramagnetic impurities, Centric Scan SPRITE MRI is developed and has shown the potential of studying the fluid distributions in porous media (Chen *et al.*, 2005). Moreover, quantitative imaging of local fluid content can be easily obtained by this technique because most fluid bearing sedimentary rocks have a single exponential transverse magnetization decay for T_2^* (Chen *et al.*, 2006).

The development of Centric Scan SPRITE MRI starts with the Single Point Imaging (SPI) method which is a pure phase encoding technique. In the SPI method, the magnetic field gradient is first turned on. Then a short broadband RF pulse (with RF pulse rotation angle, α) is applied in the presence of the gradient. A single data point is acquired on the free induction decay (FID) at each gradient step at the encoding time (t_p) after the application of the RF pulse. From Figure 2.19, the shorter the encoding time selected, the higher the signal obtained. However, there are hardware limitations that govern how short an encoding time can be used, i.e. the ring down time of the probe. The repetition time, *TR*, is the time between subsequent RF pulses at each gradient step (Barrita, 2002).

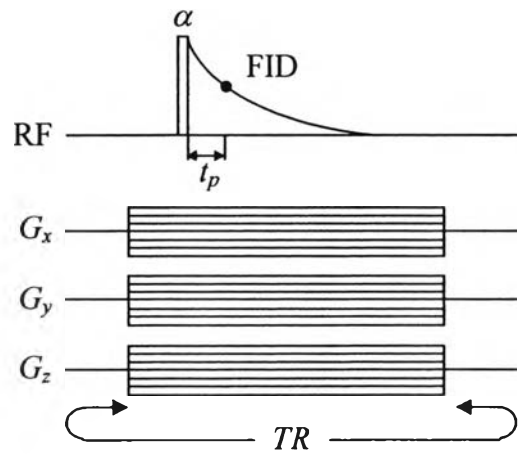

Figure 2.19 3D SPI pulse sequence (Halse, 2004)

Unlike frequency encoded images, SPI images are free from distortions due to B_0 inhomogeneity, susceptibility variations, and chemical shift. However, the drawback of the SPI method is time inefficiency since one gradient switch and RF pulse is associated with each experiment point. This limits the repetition time and

makes the imaging times long. Intense, rapid switching of the magnetic field gradients can lead to excessive gradient vibration and consequently high acoustical noise due to impulsive Lorentz forces. In addition, a period of gradient cooling is often introduced between the switching on/off of the gradients in order to maintain an acceptable gradient duty cycle over the course of the entire experiment (Halse, 2004).

Based on SPI methods, the SPRITE technique was developed to solve the previous limitations. Instead of switched on/off for each acquisition as in SPI, the phase encoding gradient is ramped in equally spaced steps which greatly reduces imaging times, minimizes gradient vibration, and also introduces T_1 contrast through partial saturation of magnetization components which have longitudinal relaxation times that are longer than the gradient switching time. In the SPRITE sequence, the gradient is ramped in discrete steps and an RF pulse is applied which includes collecting a single data point at each gradient step (Balcom *et al.*, 1996). Since the extent of gradient switching is dramatically reduced, SPRITE is an acoustically silent technique when compared to SPI. Furthermore, the demands on the gradient hardware are significantly reduced and the overall acquisition time of SPRITE can be decreased compared to SPI by employing shorter repetition times (Halse, 2004).

Figure 2.20 shows a standard 3D SPRITE imaging pulse sequence (only 16 steps are shown). Repetitive excitation and acquisition is performed in the presence of a ramped primary phase encoding gradient, G_x in this case. A single short-duration RF pulse is employed after the magnetic field gradients have been switched on and allowed to stabilize for each step. As the RF pulse is applied in the presence of a magnetic field gradient, its duration must be short enough to irradiate the overall distribution of frequencies introduced by the gradient. Meanwhile, the gradients in the second and third dimension, in this case, G_y and G_z, are incremented following each cycle of G_x leading to simple Cartesian sampling of two- and three-dimensional *k*-space (Chen *et al.*, 2005).

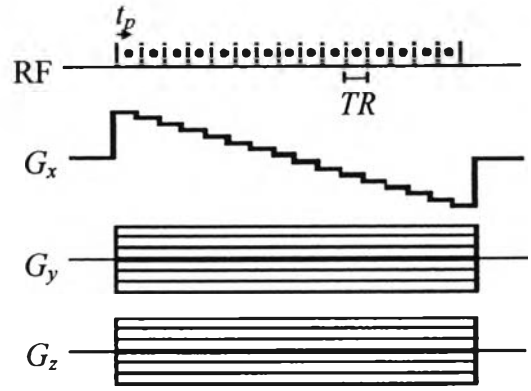

Figure 2.20 3D SPRITE pulse sequence (one gradient stepped) (Halse, 2004)

Centric Scan SPRITE is different from standard SPRITE in terms of *k*-space sampling. Standard SPRITE collects lines of *k*-space data, from one extreme through the center to the opposite extreme. For Centric Scan SPRITE techniques, data acquisition commences at the *k*-space origin and proceeds to the extremities of *k*-space. The 2D Spiral SPRITE pulse sequence is shown in Figure 2.21(a). The gradients of G_x and G_y are sinusoidally ramped yielding a spiral *k*-space trajectory as illustrated in Figure 2.21 (b) (Szomolanyi *et al.*, 2001). RF pulses are applied at each gradient level with a single FID data point acquired at phase encoding time t_p after each RF pulse. For a typical *TR* of 1 ms, a 2D image with a 64x64 matrix can be obtained in 2.5 s with a Spiral-SPRITE measurement (Chen *et al.*, 2005).

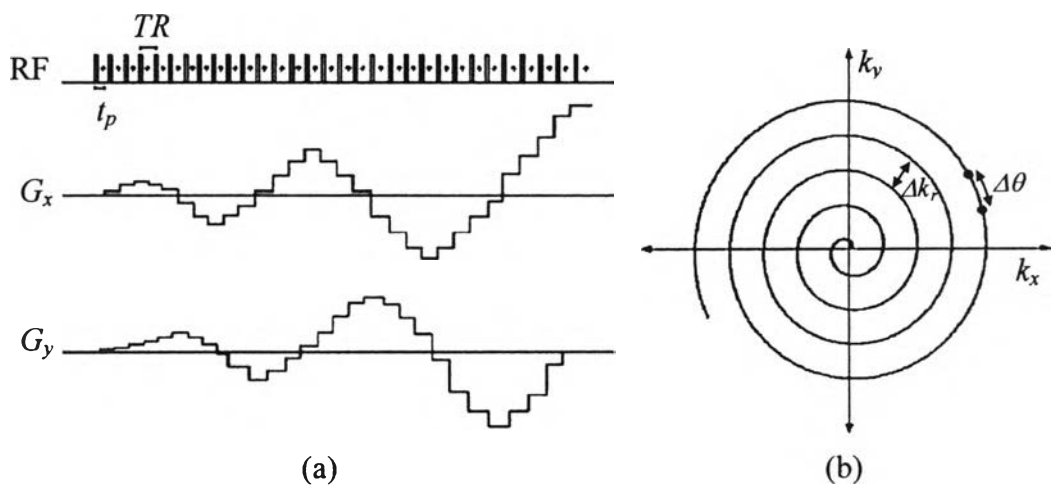

Figure 2.21 (a) 2D Spiral SPRITE pulse sequence (b) Spiral *k*-space trajectory (Halse *et al.*, 2003)

The extension to 3D requires an additional phase encode gradient in the third dimension. Since, 2D Spiral SPRITE yields the "stack of spirals" trajectory which does not begin sampling in the centre of the *k*-space cube for all spirals and is therefore not a true 3D centric scanning technique. The Conical-SPRITE technique is a 3D centric scan technique, employing a series of spiral trajectories along conical surfaces to sample the *k*-space cube. G_x and G_y are sinusoidally ramped while G_z is linearly ramped through a discrete set of gradient amplitudes for each nested cone. The data acquisition commences at the *k*-space origin and proceeds to the extremities of *k*-space. The Conical-SPRITE pulse sequence and a single conical trajectory are illustrated in Figure 2.22 (Halse *et al.*, 2003).

An RF pulse is applied at each gradient level; the repetition time (*TR*) is the time between successive RF pulses; a single FID point is sampled at a time t_p after each RF pulse. Figure 2.22 (a) illustrates the first few dozen points on a single conical trajectory as shown in Figure 2.22 (b).

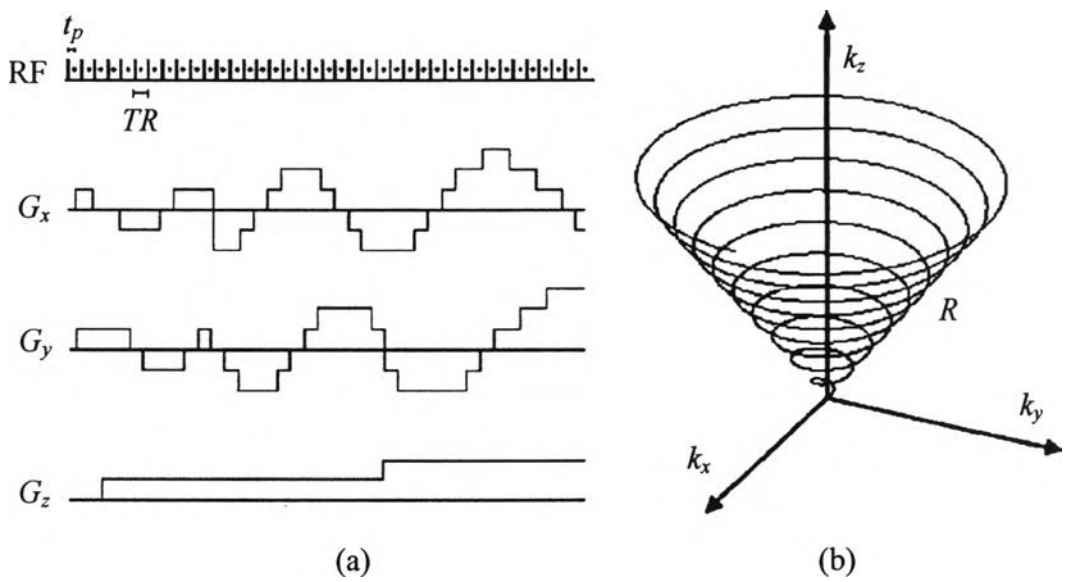

Figure 2.22 (a) 3D Conical SPRITE pulse sequence (b) Conical *k*-space trajectory (Halse *et al.*, 2003)

In practice, 39 cones are employed for sampling the 3D *k*-space cube. For a typical *TR* of 1 ms, a 3D image with a 64x64x64 matrix can be obtained in 1 min with a Conical SPRITE measurement (Chen *et al.*, 2005).

The spatially resolved signal equation in a centric scan experiment is given by:

$$S = \rho_{app} = \rho_o e^{-\frac{t_p}{T_2^*}} \sin\theta \qquad (32)$$

where S is the experimental signal, ρ_{app} is the apparent spin density, ρ_0 is the true spin density (fluid content), t_p is the encoding time (μs), T_2^* is the effective spin-spin relaxation time (ms), and θ is the RF flip angle (Halse *et al.*, 2004).

Note in Eq. (32) that $\sin\theta$ will be a constant throughout the sample. The single exponential T_2^* decay of porous media, fully or partially saturated with minimal variation with saturation level, is important for quantitative SPRITE imaging. Local fluid content determination can be achieved by acquiring a series of Centric Scan SPRITE images with different t_p, and then fitting it to Eq. (32). If the experimental parameter t_p is $<< T_2^*$ the local image intensity will be directly proportional to the local fluid content. Alternatively if T_2^* is a constant, invariant with structure and local fluid content, then the local image intensity is directly proportional to local fluid content. Furthermore, the minimal measurement deadtime in the Centric Scan SPRITE technique ensures that systems with T_2^* signal lifetimes as short as tens of microseconds may be readily imaged. For unconsolidated porous media, sand pack models, T_2^* is moderate the same and approximately constant for the whole sample because of the homogeneity of the sand pack. This technique allows the quantification of fluid distributions in a dynamic system or flood testing. For rock samples which present more heterogeneity, this information could be used as the basis for designing customized treatments to control and/or minimize conformance problems in rock formations (Chen *et al.*, 2006).

Centric Scan SPRITE MRI techniques for the study of fluids in porous media have several advantages over previous MRI SPRITE techniques. These methods are faster with better signal-to-noise ratio (SNR), and solve many of the problems encountered with short MR signal lifetime samples, and reduce instrumentation demands compared to previous techniques (Chen *et al.*, 2006).

2.9 Centric Scan SPRITE MRI Application in Porous Media

Several studies of Centric Scan SPRITE MRI techniques for porous media have been undertaken. The benefit of this technique is the quantification of fluid distribution in porous media. This following research is representative of current applications of this technique in porous media.

Marica *et al.* (2006) measured porosity of porous media using density weighted, centric scan, 3D Conical SPRITE MRI techniques. The magnitude of the ensuing MR signal is directly proportional to the amount of hydrogen present in the sample volume and provides in principle a measure of liquid-filled porosity. Sand stone samples which vary in porosity and heterogeneity were used. Centric Scan SPRITE uses a pure phase encoding of the magnetization and the local image intensity depends on T_2^* and proton density (ρ_0). Since the fluid saturation in porous media gave a single exponential T_2^* decay, the true density imaging was achieved by extrapolation of T_2^* mapping data to zero encoding time. The results showed good agreement (2 % error) with bulk gravimetric measurements (Marica *et al.*, 2006).

Chen *et al.* (2006) studied quantitative fluid distributions in sedimentary rocks. Paramagnetic impurities in the rock lead to short magnetic resonance lifetimes. Quantitative imaging of local fluid content is facilitated by single exponential transverse magnetization decay in rocks. 2.4 Tesla magnet was used with a fully water saturated Berea sandstone. By 3D Conical SPRITE MRI images, the measurements showed the single exponential T_2^* decay. This ensures that quantitative fluid-density images can be easily obtained by exponential fittings.

Li *et al.* (2007) investigated quantitative discrimination of water and hydrocarbon by using diffusion coefficient mapping. Diffusion contrast preparation incorporated into Centric Scan SPRITE MRI can be used to spatially resolve the contrast and quantify oil and water content in porous media. Polydimethylsiloxane (PDMS) was used as the oil phase, with a viscosity of 4.56 cp and a density of 0.913 g/ml. The sand pack representing the porous media had a porosity of 0.41. The results showed the high potential of this method in order to quantify local oil and water content in porous media. In addition, the diffusion mapping idea was applied to a water-

flooding experiment as a preliminary approach to quantitative oil distribution mapping during flooding processes.